minerals

MDPI

Article

Nitrogen under Super-Reducing Conditions: Ti Oxynitride Melts in Xenolithic Corundum Aggregates from Mt Carmel (N. Israel)

William L. Griffin [1,*], Sarah E. M. Gain [1,2,3], Martin Saunders [3], Olivier Alard [1], Jeremy Shaw [3], Vered Toledo [4] and Suzanne Y. O'Reilly [1]

1 ARC Centre of Excellence for Core to Crust Fluid Systems (CCFS) and GEMOC, Earth and Environmental Sciences, Macquarie University, North Ryde, NSW 2109, Australia; sarah.gain@dmirs.wa.gov.au (S.E.M.G.); olivier.alard@mq.edu.au (O.A.); sue.oreilly@mq.edu.au (S.Y.O.)
2 Geological Survey of Western Australia, Carlisle, WA 6101, Australia
3 Centre for Microscopy, Characterisation and Analysis, The University of Western Australia, Crawley, WA 6009, Australia; martin.saunders@uwa.edu.au (M.S.); jeremy.shaw@uwa.edu.au (J.S.)
4 Shefa Gems Ltd., Netanya 4210602, Israel; veredshefa@gmail.com
* Correspondence: bill.griffin@mq.edu.au

Abstract: Titanium oxynitrides (Ti(N,O,C)) are abundant in xenolithic corundum aggregates in pyroclastic ejecta of Cretaceous volcanoes on Mount Carmel, northern Israel. Petrographic observations indicate that most of these nitrides existed as melts, immiscible with coexisting silicate and Fe-Ti-C silicide melts; some nitrides may also have crystallized directly from the silicide melts. The TiN phase shows a wide range of solid solution, taking up 0–10 wt% carbon and 1.7–17 wt% oxygen; these have crystallized in the halite (fcc) structure common to synthetic and natural TiN. Nitrides coexisting with silicide melts have higher C/O than those coexisting with silicate melts. Analyses with no carbon fall along the TiN–TiO join in the Ti–N–O phase space, implying that their Ti is a mixture of Ti^{3+} and Ti^{2+}, while those with 1–3 at.% C appear to be solid solutions between TiN and $Ti_{0.75}O$. Analyses with >10 at% C have higher Ti^{2+}/Ti^{3+}, reflecting a decrease in fO_2. Oxygen fugacity was 6 to 8 log units below the iron–wüstite buffer, at or below the Ti_2O_3–TiO buffer. These relationships and coexisting silicide phases indicate temperatures of 1400–1100 °C. Ti oxynitrides are probably locally abundant in the upper mantle, especially in the presence of CH_4–H_2 fluids derived from the deeper metal-saturated mantle.

Keywords: titanium nitrides; oxynitrides; methane–hydrogen fluids; mantle mineralogy; reducing conditions; Mt Carmel

Citation: Griffin, W.L.; Gain, S.E.M.; Saunders, M.; Alard, O.; Shaw, J.; Toledo, V.; O'Reilly, S.Y. Nitrogen under Super-Reducing Conditions: Ti Oxynitride Melts in Xenolithic Corundum Aggregates from Mt Carmel (N. Israel). *Minerals* **2021**, *11*, 780. https://doi.org/10.3390/min11070780

Academic Editor: Yaoling Niu

Received: 15 June 2021
Accepted: 12 July 2021
Published: 18 July 2021

1. Introduction

Nitrogen is a minor element in Earth's mantle; it is usually regarded as a fugitive element, ultimately carried to the surface in magmas or C–O–H fluids, and diamonds. Many studies have treated its behavior under relatively oxidizing conditions, in which such fluids are dominated by CO_2 + H_2O. However, several analyses (e.g., [1–3]) suggest that the sublithospheric mantle is metal-saturated, in which case the oxygen fugacity is controlled by the iron–wüstite buffer (IW), and C–O–H fluids are dominated by CH_4 + H_2. Under such reducing conditions, N may display different lithophile/siderophile behavior, as witnessed by the occurrence of osbornite (TiN) in reduced enstatite chondrites, together with phases such as cohenite (Fe_3C) and oldhamite (CaS) ([4], references therein).

Osbornite was first reported as a terrestrial material in the ejecta of kimberlitic eruptions in the Azov area on the northern edge of the Ukrainian Shield [5], where it is accompanied by other highly reduced phases including moissanite (SiC), as well as abundant corundum. It also occurs as inclusions in chromitites from the Luobusa ophiolite of

the Yarlung-Zhangbo suture in SE Tibet [6]; the associated phases are Ti-rich corundum, moissanite and a variety of Fe–Ti silicides and carbides [7–9].

The Cretaceous pyroclastic rocks of Mount Carmel (Northern Israel) erupted from six to eight volcanic centers from 100–85 Ma, and over an area of at least 150 km^2 (Figure S1). Xenoliths and xenocrysts enclosed in these tuffs and in related alluvial deposits appear to represent snapshots of similar magma–fluid systems at different stages of their evolution. They record a wide range of oxidation states, including some of the most reducing conditions yet reported in terrestrial rocks [10,11]. Melts trapped in xenolithic corundum aggregates show melt evolution and fractional crystallization under strongly reducing conditions (fO_2 = ΔIW − 6 to − 9 [10,11]), consistent with fluxing of a magmatic system by CH_4 + H_2 fluids derived from a metal-saturated mantle [12,13]. Inclusions in corundum comprise a range of Ti-rich phases in which Ti is either trivalent (tistarite, Ti_2O_3; carmeltazite, $ZrAl_2Ti_4O_{11}$; khamrabaevite, TiC [12,14]) or divalent (TiB_2 [15]); these are associated with a range of immiscible Fe–Ti–Zr–C silicide melts and their crystallization products [16] moissanite (SiC [17]), hibonite [10] and a series of Ti nitrides and oxynitrides, the subject of this paper.

The geological setting and provenance of the samples have been discussed in detail elsewhere [18] to demonstrate that assertions of their anthropogenic origin [19] are untenable. In brief: (1) all of the mineral assemblages described in this and previous papers are found in situ in the pyroclastic rocks of Cretaceous volcanoes on the Mt Carmel plateau; (2) the alluvial deposits that also contain these xenoliths are paleoplacers that rest on bedrock at the base of Pliocene–Pleistocene terraces well above the current drainage of the Kishon River, and are overlain by 4–10 m of undisturbed sediments; (3) much of the heavy mineral assemblage, including abundant moissanite, is also found in lithified Miocene beach placers, deposited during a marine incursion that redistributed surface materials across the Yizre'el valley, now drained by the Kishon River. All of these deposits predate human occupation in the area.

Here, we present petrographic images and elemental maps to establish the relationships between nitrides, borides, carbides and silicide and silicate melts; we then present mineral chemistry and discuss the origins and evolution of these melts and the associated nitrides.

2. Methods

The sampling methods, which are designed to avoid anthropogenic contamination, have been described in detail elsewhere [11,18].

2.1. SEM, FE-SEM, EMP

Samples were mounted in epoxy blocks, polished and coated with carbon; all mounts used for the analyses presented here were cleaned and carbon-coated together. A Zeiss EVO MA15 scanning electron microscope (SEM) at the Geochemical Analysis Unit (GAU), Macquarie University, Sydney, Australia was used to capture backscattered electron (BSE) images and energy dispersive X-ray spectrometry (EDS) was used to map the elemental composition of the samples, and to analyze phases of interest. An accelerating voltage of 15 keV and a beam current of 1 nA were used. Images and qualitative EDX data were also collected at Macquarie University on an FEI Teneo field emission scanning electron microscope equipped with secondary and backscattered-electron detectors and a pair of integrated Bruker energy dispersive X-ray spectroscopy analyzers (Bruker XFlash Series 6).

Major and minor elements were determined by an electron microprobe (EMP) using a CAMECA SX100 equipped with five wavelength-dispersive spectrometers at the Macquarie University GeoAnalytical facility (MQGA; formerly GAU), Macquarie University, Sydney, Australia. Analyses were performed using a focused beam (1–2 μm) with an accelerating voltage of 15 keV and a beam current of 30 nA. Calibration standards were a suite of natural and synthetic minerals, including synthetic TiB_2, TiC, TiO and TiN. B, C, N and O were measured using a PC2 crystal (on Spectro 4). Peak counting was 30 s, and background

was counted for 15 s on either side of the peak. Oxygen and carbon were corrected for blank effects (carbon coating) by analysis of the synthetic Ti phases and Fe-Ti silicide alloys present in the analyzed samples; matrix corrections were carried out by ZAF software.

2.2. Transmission Electron Microscopy (TEM)

Focused ion beam (FIB) foils from the region of interest were prepared for TEM using two dual-beam FIB systems, an FEI Nova NanoLab 200 at UNSW and an FEI Helios G3 CX at the Centre for Microscopy Characterisation and Analysis (CMCA), the University of Western Australia, Perth, Australia. High-angle annular dark field-scanning transmission electron microscopy (HAADF-STEM) imaging and element mapping were carried out using an FEI Titan G2 80–200 TEM/STEM with ChemiSTEM Technology operating at 200 kV at the Centre for Microscopy Characterisation and Analysis (CMCA), the University of Western Australia, Perth, Australia. The element maps were obtained by EDS using the Super-X detector on the Titan with a beam size ~1 nm and a probe current of ~0.25 nA. Total acquisition times of 20–30 min were used to obtain good signal-to-noise ratios. Electron diffraction was carried out using a field-limiting aperture that selected an area approximately 400 nm in diameter. Electron energy-loss spectroscopy (EELS) was carried out using a Gatan Enfinium spectrometer at the same beam size and beam current as the EDS, and at a dispersion of 0.1 eV/pixel.

3. Results

3.1. Background

As in other xenolith studies, an idealized history of magma/fluid evolution can be constructed by piecing together information expressed in a suite of xenoliths and xenocrysts. Specifically, it is possible to arrange the samples from Mt Carmel in a sequence of progressively lower oxidation states (decreasing fO_2) that appears to record the evolution of magmas fluxed by $CH_4 + H_2$ at high fluid/rock ratios [9,10,12,20]. Grains of vesicular wüstite show fO_2 near the QFM buffer (fO_2 = ΔIW + 3 to + 4). Large euhedral to subhedral crystals of magnesian calcite have high-Sr cores with $^{87}Sr/^{86}Sr = 0.7033$, suggesting a magmatic origin, and may have crystallized near the enstatite–magnesite–olivine–diamond (EMOD) buffer (ΔIW + 1.5). Spheres of quenched Fe oxide–silicate and Ti oxide–silicate melts, many with cores of native iron (Fe^0), suggest metal/metal oxide melt immiscibility at fO_2 near IW.

Among the most common xenoliths are aggregates of skeletal/hopper crystals of corundum (Figure 1), a morphology that implies rapid crystallization from a melt supersaturated in Al_2O_3. Numerical modeling of the zoning patterns defined by Ti^{3+} concentrations [21] indicates a progression from skeletal crystallization in open-system conditions, to hopper forms in a partially closed system and finally to growth of euhedral corundum into closed melt pockets. Analysis of crystal growth rates and diffusion profiles suggests that the aggregates crystallized on very short time scales, from days to years. This rapid growth trapped pockets of Ca–Mg–Al–Si–O melts, and continuing fractional crystallization of the host corundum led to residual melts with high contents of Ti, Zr and REE. The earliest phenocrysts in these pockets are Mg–Al–Ti spinel, followed by tistarite (Ti_2O_3) and then carmeltazite ($ZrAl_2Ti_4O_{11}$) [12,14]. More evolved melts precipitated REE-rich hibonite ($CaAl_{12}O_{19}$), moissanite (SiC) and several Zr–REE phases. The melt pockets also contain a variety of immiscible carbon-rich Fe–Ti–Zr silicide/phosphide melts, mostly in the form of spherical droplets; these crystallized TiC, SiC, TiB_2 and Ti oxynitrides and a range of silicide phases [16]. Crystals of moissanite (up to 4 mm) contain inclusions of Si^0 melts that crystallized Fe, Ca and Al silicides [17].

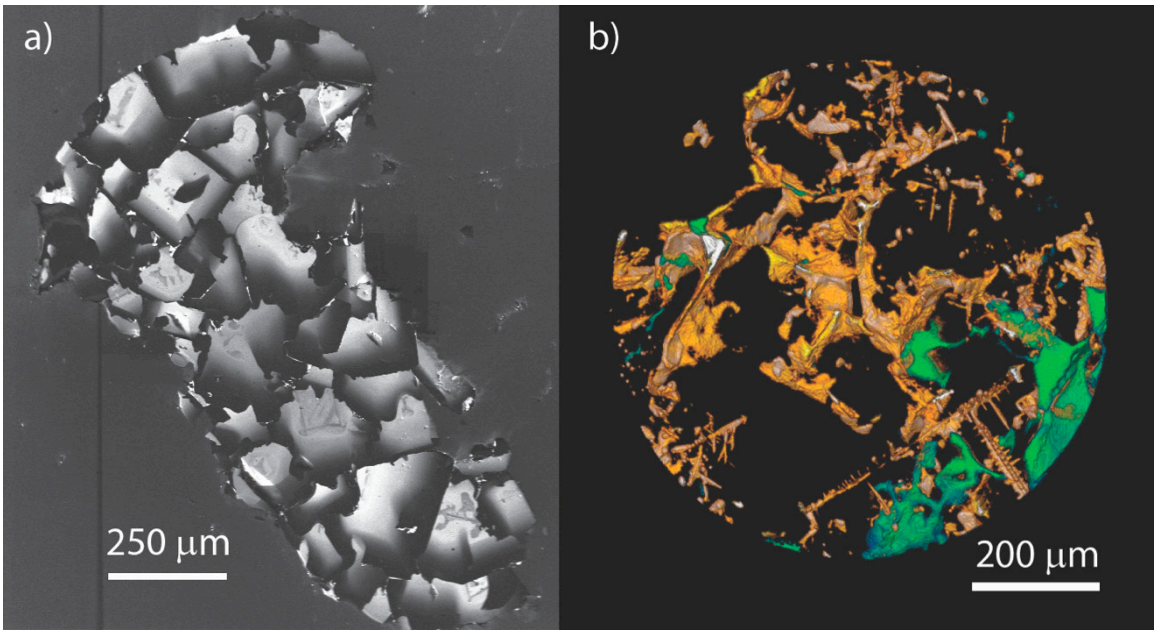

Figure 1. (**a**) Cathodoluminescence (CL) image of a corundum aggregate showing intense zoning related to Ti^{3+} concentration. Pale areas with skeletal structure have low contents of Ti and pale pink CL, which is progressively extinguished as Ti concentrations rise toward grain boundaries and pockets of trapped silicate melts. (**b**) A 3D-µCT image of a slice through a corundum aggregate. Black = corundum crystals; green = void spaces; orange = silicate melts; brighter colors = silicides and Ti nitrides.

The crystallization of SiC and the reduction of Ti^{4+} to Ti^{3+} require $fO_2 = \Delta IW - 6$ to -7 [12,17]. The most evolved silicate melts produced coarse-grained hibonite+grossite+spinel aggregates with inclusions of V^0, requiring $fO_2 \leq \Delta IW - 9$ [11]. Even lower fO_2 may be indicated by the presence of Ti^{2+}-bearing phases such as TiB_2 [15]. The most reduced conditions imply a hydrogen-dominated atmosphere, which has been confirmed by the discovery of VH_2 [22,23] and the presence of abundant H_2 in the hibonite crystals that carry inclusions of V^0 [10,11].

Paragenetic studies [9,10,20] suggest that these xenocrysts formed at ca. 1 GPa, close to the crust–mantle boundary, and crystallized over a *T* range of approximately 1450 °C to 1150 °C. Dating of zircon xenocrysts from the pyroclastic rocks [13] suggests that the crust was underplated by mafic magmas from ca. 285–100 Ma and that these melts differentiated far enough to crystallize large zircons and the typical "basaltic" sapphire found in the tuffs and alluvial deposits. We have suggested previously that volumes of these syenitic (*s.l.*) residual melts in the underplate were reduced by interaction with mantle-derived $CH_4 + H_2$ fluids [20], prior to entrainment in the Cretaceous host basalts. The detailed origin and evolution of the reduced melts will be discussed elsewhere.

3.2. Petrography

The Ti nitrides (hereafter TiN) are abundant within the corundum aggregates, and appear in a remarkable array of morphologies: small isolated globular to cruciform inclusions in corundum (Figure 2); irregular blobs, drop-shaped lenses and cruciform inclusions in silicate melts (Figures 3 and 4); long arrays or lattice patterns, apparently controlled by the orthogonal voids in the skeletal structure of the corundum crystals (Figures 4b and 5); and irregular bodies interstitial to corundum crystals with faces that may be either smooth or dentate (Figure 6). Some nitrides occur as apparent crystals on the rims of balls of Fe–Ti silicide melts, often together with TiB_2 [15] and/or TiC [16]; others clearly are immiscible with the Fe–Ti–silicide melts (Figures 6 and 7).

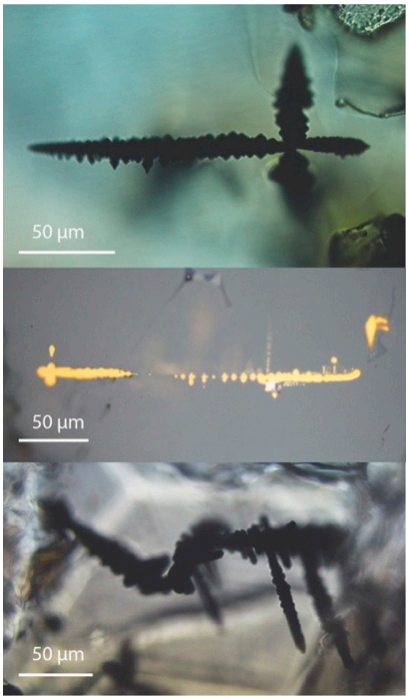

Figure 2. Microscope images of Ti nitride filling skeletal cavities in corundum. (**upper and lower panels**) Transmitted light; (**middle panel**) reflected light.

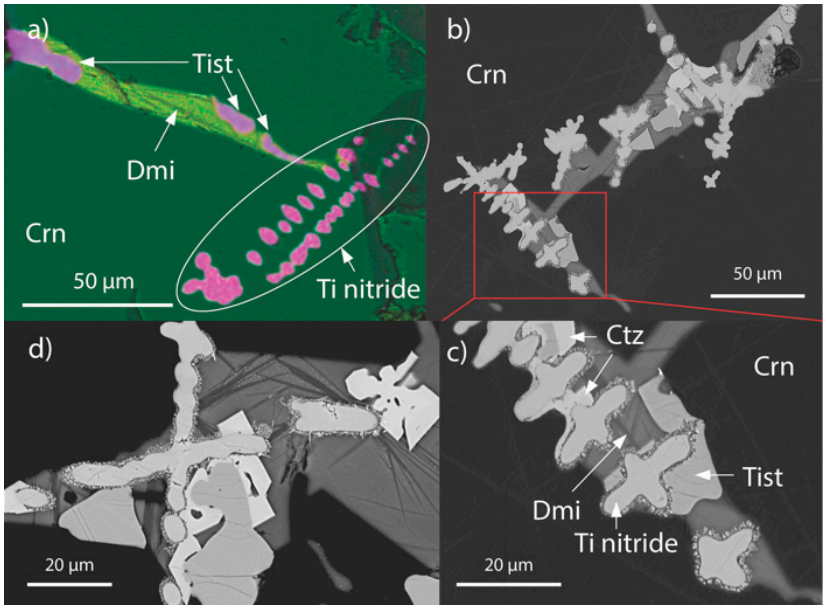

Figure 3. (**a**) SEM-EDS phase map showing silicate melt pocket in corundum, and trains of Ti nitride inclusions outlining an earlier skeletal cavity system, necked down by continued growth of the corundum. (**b**) BSE image showing Ti nitrides intersecting an interstitial silicate melt pocket in corundum, breaking down into spheroidal and cruciform blobs. (**c**) Enlargement of (**b**), showing emulsion of Ti nitride in silicate glass separating Ti nitride blobs from silicate melt. Oxide phases appear to wrap around the nitride bodies, but this may be a sectioning effect. (**d**) BSE image of elongated Ti nitride bodies in the process of necking down into individual circular bodies. Development of emulsion rims appears to postdate crystallization of carmeltazite against the nitride bodies in some places. Abbreviations: Crn, corundum; Ctz, carmeltazite; Dmi, dmisteinbergite (identified by Raman spectrum; a polymorph of anorthite ($CaAl_2Si_2O_8$); Tist, tistarite.

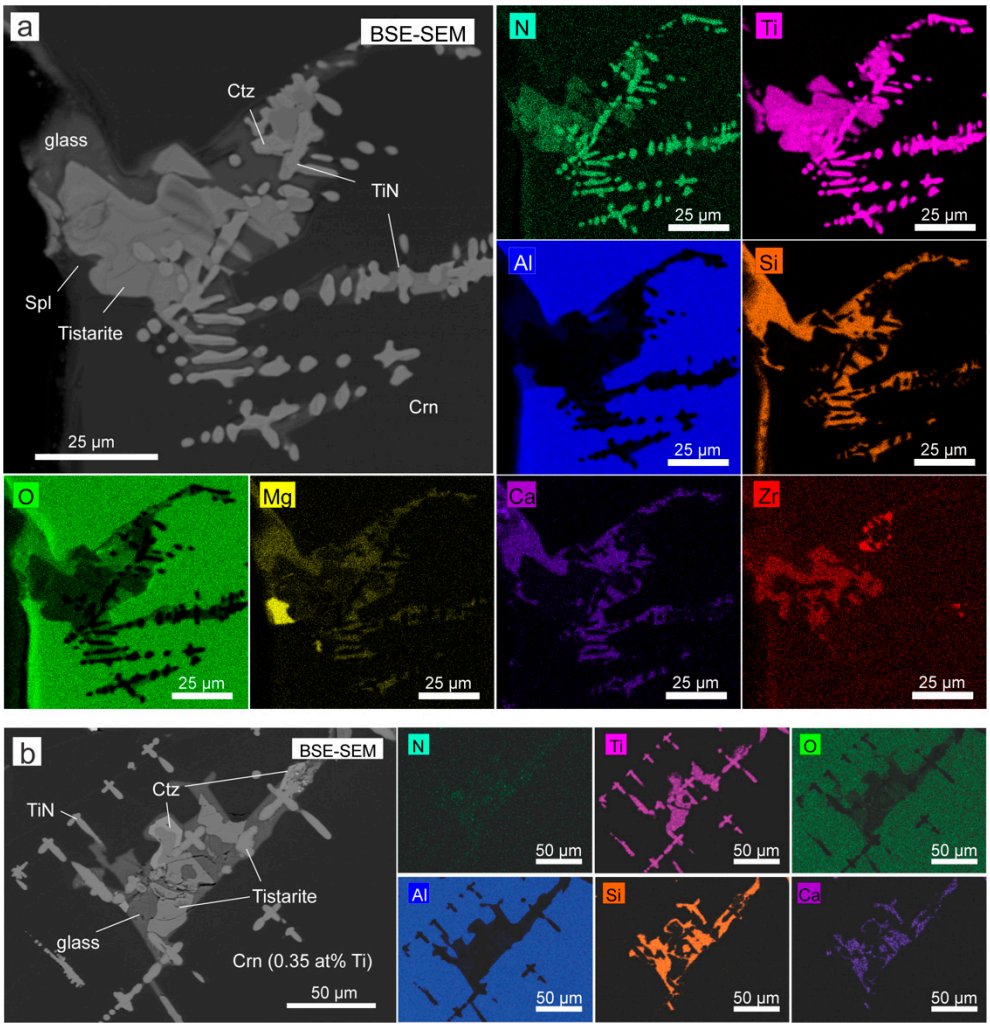

Figure 4. (**a**) BSE image and elemental maps of Ti nitride lenses in melt pockets, apparently necking down in two directions. (**b**) BSE image and elemental maps showing TiN apparently filling voids in the orthogonal structure of the skeletal corundum crystal, and necking down through further growth of the corundum. After [12]. Ctz = carmeltazite ($ZrAl_2Ti_4O_{11}$).

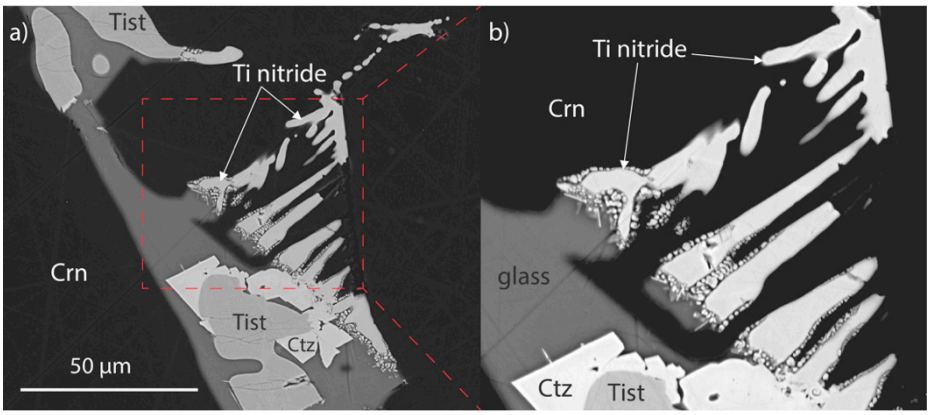

Figure 5. (**a**) BSE image of Ti nitrides filling voids in the outer part of a skeletal corundum crystal and interacting with silicate melt at the edges of a melt pocket. (**b**) Enlargement of (**a**), showing development of emulsion rims at contact between nitride in contact with silicate glass but not in contact with corundum.

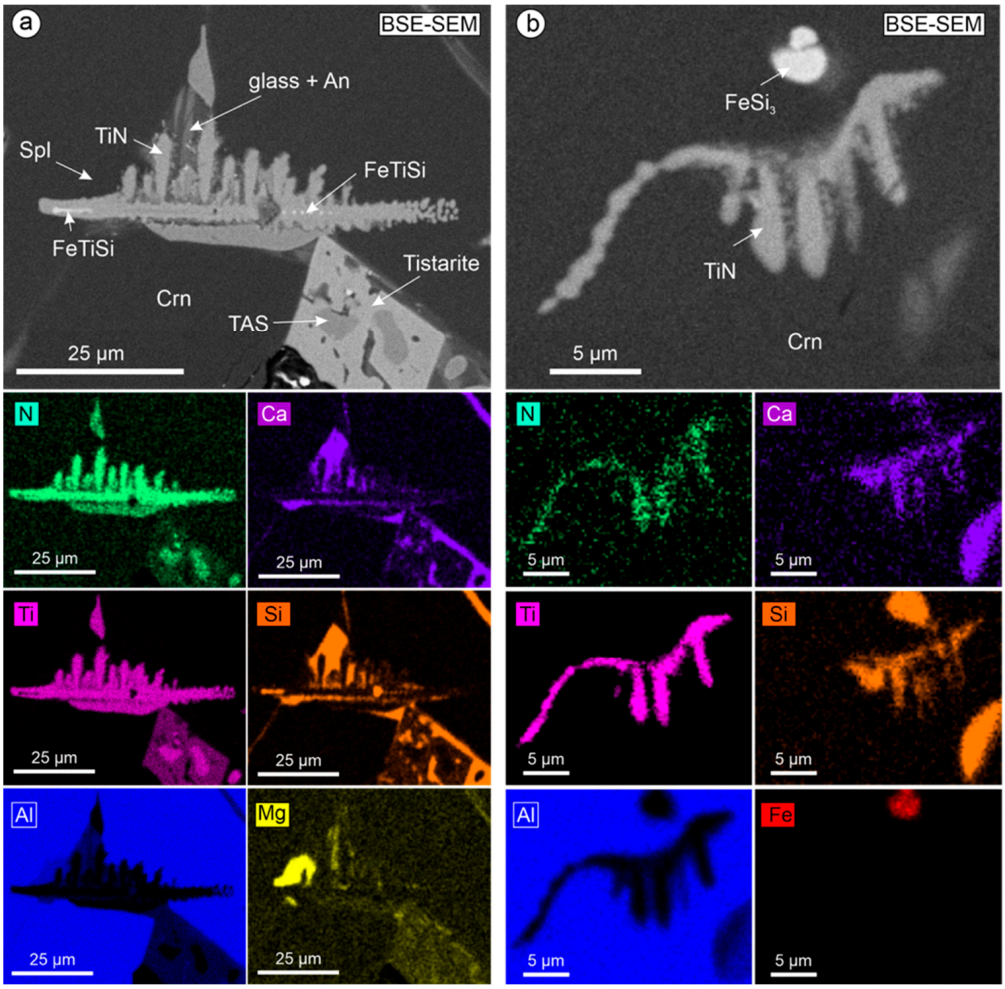

Figure 6. (**a**) BSE image and element maps of a branching Ti nitride lens with immiscible blebs of Fe silicide across the center. Note emulsion rims on vertical branches in contact with silicate glass, but not against tistarite. (**b**) BSE image and element maps of Ti nitride filling a branched interstitial space between dentate corundum crystals; each part of the Ti nitride structure is surrounded by silicate glass. Bright blob is $FeSi_3$ melt. Crn = corundum; Spl = spinel.

The chains of evenly spaced blobs and crosses of Ti nitrides within the silicate melt pockets, and in some long arrays in the skeletal cavities (Figure 4), suggest the necking down of originally elongated or lens-shaped inclusions of a trapped fluid [24]. Nitrides in contact with silicate glass are commonly rimmed by a zone of tadpole-shaped blebs of TiN mixed with the silicate glass, or included in late-crystallizing phases (Figures 3c,d, 5, 8 and 9). Oxides (tistarite, carmeltazite, spinel) crystallizing from the silicate melt may be in direct contact with the TiN, or separated from it by a similar rim (Figures 3, 5, 8 and 9). TiN in contact with corundum seldom shows such rims (Figures 3 and 5).

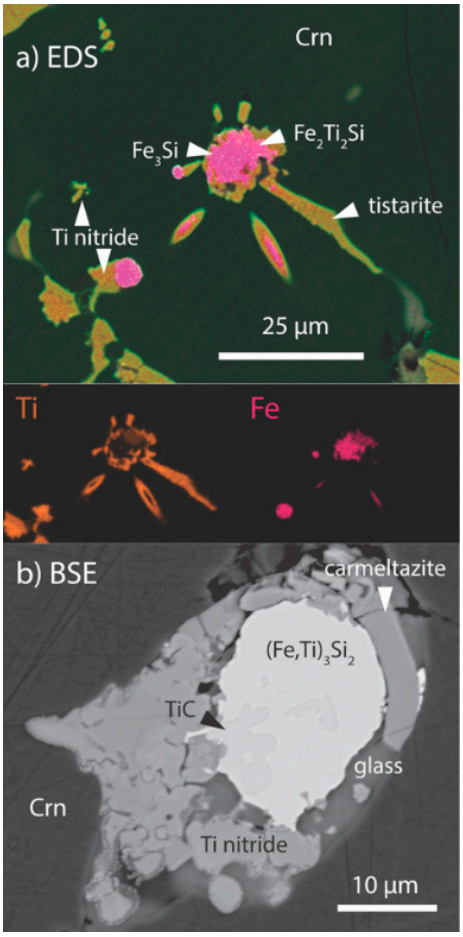

Figure 7. (**a**) BSE image with Ti and Fe maps, of a branching Ti nitride lens with immiscible blebs of Fe silicide across the center. Note emulsion rims on vertical branches in contact with silicate glass, but not against tistarite. (**b**) BSE image of Fe–Ti–silicide spheroid in a melt pocket, which also contains khamrabaevite (TiC), carmeltazite and irregular blobs of Ti nitride; the microstructures suggest the presence of three immiscible melts. Crn, corundum.

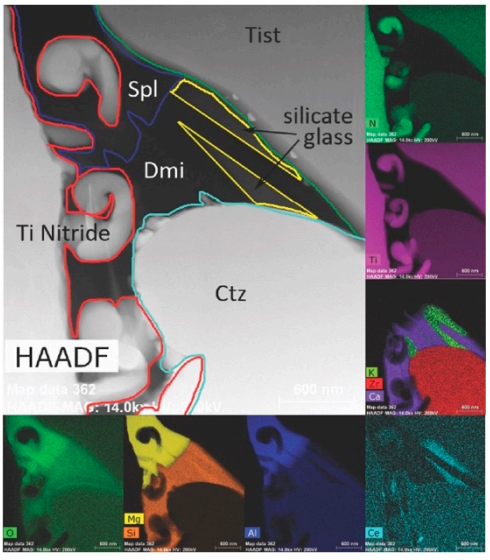

Figure 8. TEM image and element maps of contact between Ti nitride and a silicate melt pocket containing carmeltazite (Ctz) and quench crystals of dmisteinbergite (Dmi; anorthite polymorph) in silicate glass. Spl, spinel.

Table 1. Summary of populations.

Morphology	*n*	Weight %			Atomic %			Mean	Mean
		C	N	O	C	N	O	Ti/(N, O, C)	N/(O + C)
small, low-C	12	0.9	17.1	6.3	2.3	37.4	12.1	0.93	3.3
small, high-C	11	5.4	13.7	5.1	13.3	29.2	9.6	0.92	1.4
large interstitial	8	0.8	15.4	9.3	2.0	33.0	17.5	0.90	1.8
silicate melts	28	0.9	15.7	8.6	2.3	34.0	16.2	0.90	2.3
with silicides	17	5.6	12.2	6.9	13.9	26.0	12.9	0.89	1.1
void fillings low-C	5	1.3	15.0	8.6	2.7	33.0	16.2	0.92	2.4
void fillings high-C	6	6.1	11.9	8.1	14.9	25.1	14.5	0.83	1.0

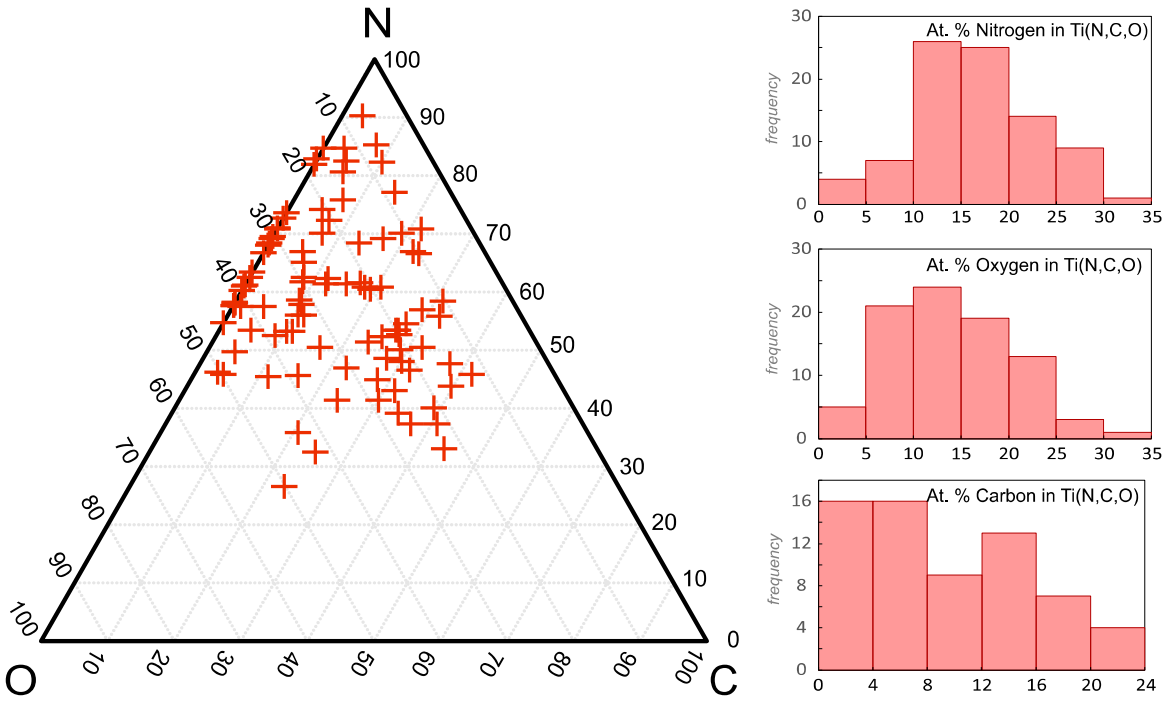

Figure 9. (**Left**) Ternary plot illustrating overall negative correlation between C and N contents over a range of O contents. (**Right**) Histograms showing abundances of N, O and C in the analyzed Ti nitrides, classified according to paragenesis (Table 1).

3.3. Mineral Chemistry and Structure

EMP analyses of Ti–N phases (Table S1) are summarized in Table 1 and Figures 9 and 10. The Ti–N phase shows a wide range of solid solution, taking up 0–10 wt% carbon and 1.7–17 wt% oxygen. Most of the analyses have 20–35 at.% N and 8–20 at.% O and more than half have >10 at% C. There is a broad negative correlation between N and C over a range of 20 at.% O (Figure 10); the Ti–N phase is best described as a carbon-bearing Ti oxynitride $Ti_x(N,O,C)_{2-x}$ where X varies from 0.74–1.04 (mean and median = 0.90, stdev = 0.08). The range of TiN–TiO substitution is only slightly larger than that observed by [25] in thin films.

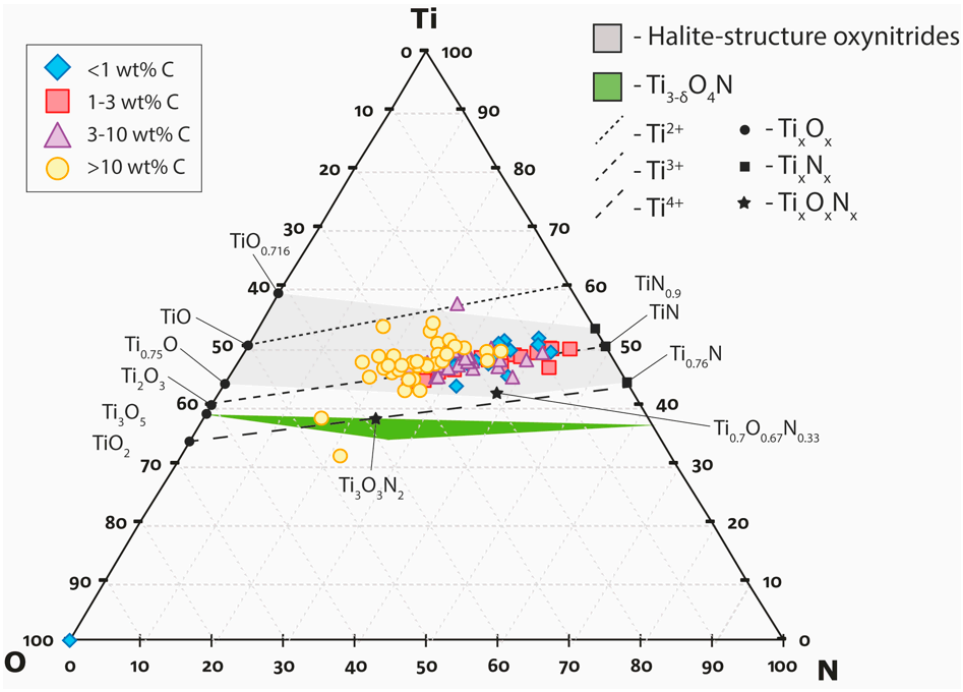

Figure 10. Phase space of Ti oxynitrides, after [25], showing distribution of analytical data; individual points are color-coded to show carbon contents. Phases in the green field would have a pseudo-brookite structure. Dashed and dotted lines define substitutions of Ti^{2+}, Ti^{3+} and Ti^{4+}; the scatter of analytical data suggests that Ti is Ti^{3+} in most grains, and a mix of Ti^{3+} and Ti^{2+} in others.

The most consistently present minor element is V, with a mean value of 0.16 wt% and a maximum of 1.1 wt%; other minor elements (Cr, Al, Fe, Mn, Si) are typically below 0.1 wt%.

There is a broad correlation between paragenesis and composition (Table 1), although the paragenesis of some nitrides is uncertain because of the effects of 2D sectioning of 3D structures. Nitrides occurring as blebs or crosses in silicate glasses nearly all have <5 at.% C (0–7.4%, mean 2.3%) and <15 at.% O (3.3 to 7.8 %, mean 16.2 wt%), and this is true also of most large interstitial nitrides (mean C = 2.0 at.%; mean O = 17.5 at.%). In contrast, nitrides associated with silicides ± TiB_2 have much higher contents of carbon (5–23.1 at.%, mean 13.9 at.%) and lower contents of oxygen (7–24 at.%, mean 12.9 at.%). Nitrides filling skeletal cavities in the corundum show a distinct bimodal distribution (Table 1) corresponding to the two silicate-related and silicide-related populations. Small isolated inclusions also show a broadly bimodal distribution of compositions, falling equally into low-C/high-O and high-C/low-O populations (mean C = 2.3 and 13.3 at.%; mean O = 12.1 and 9.6 at.%, respectively; Table 1). The proportions of analyses in the two populations are not necessarily representative of their relative abundances in the system as a whole, because larger inclusions were preferentially analyzed. The EMP data (Table S1) also include a number of analyses with Ti between ca. 75 wt% and 67 wt%, suggesting the analysis of fine-grained mixtures of Ti(N,O,C) with another phase. One end member of this distribution is represented by a group of analyses with a mean of 69 wt% Ti and an empirical formula of $Ti_2(N_{0.43}O_{0.43}C_{0.14})_3$ (Table 1).

TEM-EDS analysis of a nitride phase coexisting with TiB_2 shows it to be $Ti(N_{0.57}O_{0.17}C_{0.09})$ (Table 1). The Ti–N phase shown in Figure 9, which appears to have been a melt immiscible with the host silicate melt, has the empirical formula $Ti(N_{0.50}O_{0.45}C_{0.05})$ (TEM-EDS analysis). Both examples have electron diffraction patterns (Figure S2) consistent with the halite structure (fcc) common to TiN, with a_0 = 4.3–4.4 Å (*cf* synthetic TiN a_0 = 4.242 Å).

4. Discussion

4.1. Valence State of Ti in Ti(N,O,C)

The phase space of the relevant part of the Ti–N–O system [25] is shown in Figure 10. The ternary space is dominated by a field in which all compositions can crystallize as solid solutions ($Ti_xN_yO_z$) with the rock–salt structure. The defect chemistry of this structure allows this wide range of compositions and accommodates a range in the oxidation state of Ti, from Ti^{3+} in TiN to Ti^{2+} in TiO. The data reported here define a coherent range within that space.

Analyses with no detectable carbon fall along the TiN–TiO join, implying that their Ti is a mixture of Ti^{3+} and Ti^{2+}, while those with 1–3 at.% C define a trend parallel to, but slightly above, the Ti^{3+} boundary, consistent with solid solution between TiN and $Ti_{0.75}O$. This suggests that fO_2 was in the range $\Delta IW - 6$ to $- 8$, with the lower value corresponding to the Ti_2O_3–TiO buffer. A major cluster of points with ca. 3–10 at.% C (mean 7 at.%) scatters more toward the TiO–TiN join. Analyses with >10 at% C generally correspond to nitrides that coexist with Fe–Ti silicides, and scatter more widely between the Ti^{3+} and Ti^{2+} boundaries. The apparent higher abundance of Ti^{2+} in the higher-carbon nitrides may reflect a decrease in fO_2 during the exsolution of nitride melts from the silicide melts. If so, this would be consistent with the overall trend of fO_2 during the evolution of the Mt Carmel magmatic "system", which ends with the precipitation of the hibonite+grossite+V^0 assemblage ($fO_2 = \Delta IW \leq -9$ [10,11,22]).

The suggested "end member" phase $Ti_2(N,O,C)_3$ described above does not appear in the analysis by [25] (Figure 11); however, Ti_2N_3 is a common synthetic product used in thin-film surface coatings. The observed example may represent a subsolidus breakdown product of the dominant Ti(N,O,C) phase.

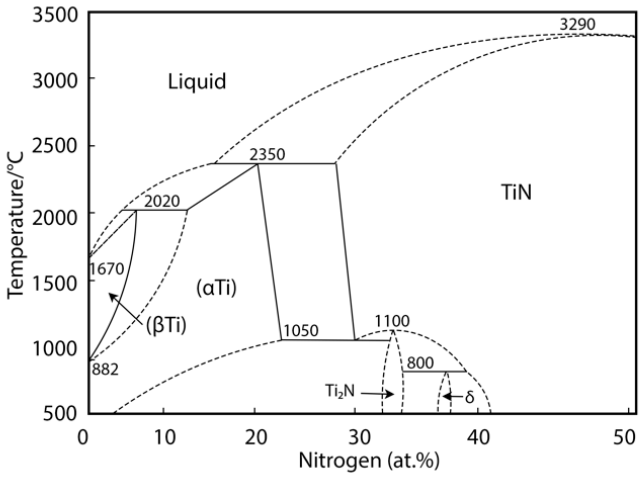

Figure 11. Ti–N phase diagram, 1 atm. pressure. Modified from [26–28].

4.2. Evolution of the Ti(N,O,C) Melts

The petrographic observations (Figures 2–8) indicate that the rapidly growing corundum aggregates trapped three types of mutually immiscible melts: Fe–Ti–C silicide, Ca–Al–Mg silicate, and Ti(N,O,C). The bimodal distribution of C–O contents in the oxynitride melts (Table 1) suggests that some were in at least partial equilibrium with silicide melts, and others with silicate melts. This implies local equilibrium in chemically restricted environments, probably corresponding to melt pockets dominated by either silicide melts or silicate melts. Such local environments would be created by the rapid growth of the surrounding corundum crystals, which resulted in the necking off of larger melt pockets into smaller ones, with the silicide melts being in many cases physically isolated from the silicate melts.

Petrograph observations (Figures 3 and 9) also indicate that exsolution of nitride melts from the silicate melts occurred before or simultaneously with the nucleation of the first

oxide phases, tistarite (Ti_2O_3) and Mg–Al spinel. The degree of substitution of Al for Mg in these spinels [12] is consistent with *T* of 1450–1400 °C, while the crystallization of tistarite requires fO_2 = ca. ΔIW − 7. The conditions for exsolution of nitride melts and crystallization of nitrides from Fe–Ti silicides are less well constrained, but probably lie in the same range [16].

The solubility of N in silicate melts is strongly correlated with pressure up to ca. 3 GPa, but increasing temperature leads to a drop in N solubility [29]. The main factors controlling N solubility in silicate melts at lower pressures are fO_2 and melt composition [30], which affect N speciation. Under oxidizing conditions, N is physically dissolved in silicate melts as N_2, even in the presence of water. Near the MW buffer, it is present as NH^{2+} and NH_3 complexes if water is present, but as N_2 in the absence of water. At and below the fO_2 of the IW buffer, COH fluids are dominated by CH_4 and H_2, leading to the presence of NH^{2-} groups [30,31]. The solubility of N in silicate melts increases by five orders of magnitude as fO_2 drops from IW to ΔIW − 8 and N becomes chemically bonded in the silicate melt network as N^{3-} species [32].

The solubility of N in the Fe–Ti–Si–C metallic melts is less well understood, because most experimental work is limited to Fe or Fe–N ± C systems, relevant either to the formation of Earth's core or to steelmaking. Increasing *T* leads to decreased solubility of N in Fe-rich melts [33]. However, several experimental studies have observed the high-*T* (ca 1500 °C) exsolution of a "N-rich fluid" from melts in the Fe–N and Fe–C–N systems, and shown that the exsolved melts re-dissolved when *T* was increased [29,33,34]. The implied increase in N solubility with increasing *T* may reflect the presence of high levels of carbon in the experiments; higher C or Si in the melt lowers N solubility, as both elements are more siderophile at low fO_2 and in effect "eject" the N as an immiscible N-rich melt.

In these experiments, the solubility of N in the metallic melts was on the order of 1–2 wt% at 1 GPa and increased strongly with increasing *P*. In contrast to similar experiments on silicate melts, N solubility in the Fe-rich melts decreased markedly as fO_2 was lowered to ΔIW − 3.7. Estimates of $D_N^{\text{metal melt/silicate melt}}$ at pressures <4 GPa suggest a drop from 10–30 at ΔIW − 1 [29,33] to 2.9 at ΔIW − 2.4 and to 0.5 at ΔIW − 3.3 [35], i.e., N becomes significantly more lithophile as fO_2 decreases below the IW buffer. However, the sparse observations of TiN apparently crystallizing on the rims of Fe–Si melt spherules (Figure 7) suggest the presence of some N in the Fe–Si melts. As cooling at constant fO_2 would only increase the solubility of N in the metallic melt, the expulsion of TiN from the silicide melts can probably be ascribed to the effect of decreasing fO_2.

These experimental data suggest that when the corundum aggregates at Mt Carmel began to crystallize at fO_2 = ΔIW − 6 to − 7, *T* ca. 1450 °C and *P* ca. 1 GPa [12], partition coefficients $D_N^{\text{metal melt/silicate melt}}$ would have been << 1, and N would be largely dissolved in the silicate melts rather than in the coexisting metallic melts. In this case, the cause of the immiscibility of the Ti(N,O,C) melts is not obvious, because both declining *T* and decreasing fO_2 would only lead to higher N solubility in the silicate melts; another trigger appears to be required.

Our modeling of the zoning patterns in the skeletal corundum crystals (Figure 1; [21]) shows a progressive change from rapid crystal growth in an open system, with a moving (i.e., constant composition) melt/fluid, to more sedate growth as the system became less porous, and finally to exponential reduction of melt volumes as individual pockets were isolated from the circulating melt. The corundum aggregates, at least in the early stages, formed a dynamic open network in which the size and shape of void spaces were continually changing as the crystals grew. If nitrogen was being supplied (along with Al_2O_3, C and H) by the moving melt/fluid, then the melt pockets may have been accumulating N even as melt volumes shrank, eventually leading to saturation in N and the expulsion of an immiscible N-rich fluid [34]. Martinez and Javoy [36] have pointed out that TiN is the most easily formed nitride, and that N appears to have an affinity for Ti at any mantle *T*–*P*–fO_2 conditions. In the Mt Carmel corundum aggregates, Ti phases are abundant, and the trapped melts typically contain several wt% Ti [12,21]. It is therefore expected that

saturation of N in the silicate melts could trigger the release of N and the formation of immiscible Ti–N melts. Conversely, the triggering factor may have been saturation of the silicate melts in Ti, leading Ti^{3+} to couple with N^{3-} complexes present in the silicate melt to form Ti–N melts [31].

The emulsions of Ti nitride "tadpoles" (Figures 3, 5 and 8) appear to represent an interaction between nitride and silicate melts. Where these emulsions are in contact with silicate glasses, they could also reflect a late, and probably disequilibrium, process. As noted above, the solubility of N in silicate melts decreases rapidly with decreasing *P*, especially below 1–2 GPa. This suggests that the formation of the emulsions could reflect the expulsion of N from the silicate melts during the eruption of the host magma. The distribution of the "tadpoles" along the margins of larger Ti nitride inclusions in the silicate glass may indicate that N contents in the silicate melts were higher in the vicinity of the exsolved Ti nitride melts at the beginning of eruption, thus localizing the exsolution of the remaining dissolved N. With modeled time scales on the order of days to years for the evolution of the corundum aggregates [21], equilibrium was probably difficult to attain. Explosive eruption and quenching of the melts would have been very rapid, preventing microstructural equilibration.

The phase diagram for the Ti–N binary (Figure 11; [26–28]) shows Ti_xN_{1-x} as a liquidus phase at $T > 2350$ °C (1 atm). This is ca. 1000 °C above the temperatures registered by the metal alloy melts in the corundum aggregates (ca. 1500–1200 °C [16]). We have not found information on the melting points of Ti oxynitrides in the literature. Neumann et al. [37] reported complete miscibility between TiC, TiN and TiO in the solid state from 1100 °C to 1500 °C, but the presence of abundant H in the system at these low-oxygen fugacities can be expected to lower liquidus temperatures substantially. For example, small proportions of H can lower the melting point of Ti by up to 600 °C [38]. Vapor-deposited films of Ti(N,O) are stable under a hydrogen plasma, but show advanced etching at temperatures near 1100 °C [39], which may suggest that the melting point is not a great deal higher.

In the binary system, the Ti_2N phase found in one TEM-FIB foil (Table S1) can be produced by breakdown of the subsolidus Ti_xN_y phase below 1100 °C ([27], Figure 11), and this single observation may suggest the temperatures reached in some parts of the corundum aggregate–melt system before eruption of the host volcanic rocks.

5. Conclusions

The Ti(N,C,O) phases in the corundum–aggregate xenoliths from the Mt Carmel volcanoes represent immiscible melts that coexisted with mutually immiscible silicate and silicide melts under highly reducing conditions ($fO_2 = \Delta IW - 6$ to -7). Nitrides with high C/O apparently exsolved from, and/or crystallized from, silicide melts while those with lower C/O coexisted with silicate melts. Exsolution of Ti(N,O,C) from silicide melts was probably driven by falling fO_2, as N became more lithophile. Immiscibility between nitride and silicate melts may have been driven by scavenging of N from coexisting C–H–O fluids, or by saturation of Ti^{3+} as fractional crystallization of corundum reduced the volumes of trapped silicate melts. The P–T–fO_2 conditions reflected in the Mt Carmel xenolith assemblages appear to reflect interaction between small volumes of differentiated mafic melts and CH_4–H_2 fluids derived from a metal-saturated mantle. Similar assemblages have been recorded from other examples of explosive volcanism [9,20] and provide insights into the behavior of nitrogen under reducing conditions in the deeper mantle.

Supplementary Materials: The following are available online at https://www.mdpi.com/article/10.3390/min11070780/s1, Figure S1: Maps showing the regional setting of the Mt Carmel area (a) and the simplified geology with locations of Cretaceous primary volcanic vents; Figure S2: Selected area electron diffraction patterns from two zone axes obtained by tilting the same grain of the titanium nitride phase; Table S1: EMP analyses of Ti oxynitrides; Video S1: #D-μCT image of a slice through a corundum aggregate.

Author Contributions: Conceptualization, W.L.G., V.T. and S.Y.O.; methodology, W.L.G., S.E.M.G., M.S., O.A. and J.S.; analysis, S.E.M.G., M.S., O.A., J.S. and W.L.G.; resources, W.L.G., V.T. and S.Y.O.; visualization, S.E.M.G. and J.S.; data curation, S.E.M.G.; writing—original draft preparation, W.L.G.; writing—review and editing, W.L.G., S.E.M.G., V.T. and S.Y.O.; project administration, W.L.G.; funding acquisition, W.L.G. and S.Y.O. All authors have read and agreed to the published version of the manuscript.

Funding: This research was funded by the ARC National Center of Excellence for Core to Crust Fluid Systems, grant "TARDIS".

Data Availability Statement: All data are presented in Table 1 and Supplementary Materials.

Acknowledgments: We thank Dima Kamenetsky for useful arguments and providing images used in several of the figures, and Montgarri Castillo-Oliveira for assistance with figures. W.L.G. and S.Y.O. acknowledge the research funds for the TARDIS Project provided by the ARC Centre of Excellence for Core to Crust Fluid Systems. Instruments used at Macquarie University are funded by DEST Systemic Infrastructure Grants, ARC LIEF, NCRIS/AuScope, industry partners and Macquarie University. We also acknowledge the scientific and technical assistance of Microscopy Australia at the Centre for Microscopy, Characterization and Analysis, a facility funded by the University of Western Australia, and State and Commonwealth Governments. This is contribution 1668 from the ARC Centre of Excellence for Core to Crust Fluid Systems and 1468 from the GEMOC Key Centre.

Conflicts of Interest: The authors declare no conflict of interest. The funders had no role in the design of the study; in the collection, analyses, or interpretation of data; in the writing of the manuscript, or in the decision to publish the results.

References

1. Frost, D.J.; McCammon, C.A. The redox state of Earth's mantle. *Ann. Rev. Earth Planet. Sci. Lett.* **2008**, *36*, 389–420. [CrossRef]
2. Rohrbach, A.; Ballhaus, C.; Golla–Schindler, U.; Ulmer, P.; Kamenetsky, V.S.; Kuzmin, D.V. Metal saturation in the upper mantle. *Nature* **2007**, *449*, 456–458. [CrossRef]
3. Stagno, V.; Ojwang, D.O.; McCammon, C.A.; Frost, D. The oxidation state of the mantle and the extraction of carbon from Earth's interior. *Nature* **2013**, *493*, 84–88. [CrossRef] [PubMed]
4. Larimer, J.W. An experimental investigation of oldhamite, CaS; and the petrological significance of oldhamite in meteorites. *Geochim. Cosmochim. Acta* **1968**, *32*, 965–982. [CrossRef]
5. Tatarintsev, V.I.; Sandomirskaya, S.M.; Tsymbal, S.N. First finding of titanium nitride (osbornite) in Earth's rocks. *Dokl. USSR* **1987**, *296*, 1458–1461.
6. Dobrzhinetskaya, L.F.; Wirth, R.; Yang, J.; Hutcheon, I.D.; Weber, P.K.; Green, H.W. High-pressure highly reduced nitrides and oxides from chromitite of a Tibetan ophiolite. *Proc. Natl. Acad. Sci. USA* **2009**, *106*, 19233–19238. [CrossRef]
7. Xu, X.; Yang, J.; Chen, S.; Fang, Q.; Bai, W.; Ba, D. Unusual mantle mineral group from chromitite orebody Cr-11 in Luobusa ophiolite of Yarlung-Zangbo suture zone, Tibet. *J. Earth Sci.* **2009**, *20*, 284–302. [CrossRef]
8. Zhang, R.Y.; Yang, J.-S.; Ernst, W.; Jahn, B.-M.; Iizuka, Y.; Guo, G.-L. Discovery of in situ super-reducing, ultrahigh-pressure phases in the Luobusa ophiolitic chromitites, Tibet: New insights into the deep upper mantle and mantle transition zone. *Am. Mineral.* **2016**, *101*, 1285–1294. [CrossRef]
9. Xiong, Q.; Griffin, W.L.; Huang, J.-X.; Gain, S.E.M.; Toledo, V.; Pearson, N.J.; O'Reilly, S.Y. Super-reduced mineral assemblages in "ophiolitic" chromitites and peridotites: The view from Mt Carmel. *Eur. J. Mineral.* **2017**, *29*, 557–570. [CrossRef]
10. Griffin, W.L.; Gain, S.E.; Huang, J.; Saunders, M.; Shaw, J.; Toledo, V.; O'Reilly, S.Y. A terrestrial magmatic hibonite-grossite-vanadium assemblage: Desilication and extreme reduction in a volcanic plumbing system, Mount Carmel, Israel. *Am. Mineral.* **2019**, *104*, 207–219. [CrossRef]
11. Griffin, W.; Gain, S.; Cámara, F.; Bindi, L.; Shaw, J.; Alard, O.; Saunders, M.; Huang, J.-X.; Toledo, V.; O'Reilly, S. Extreme reduction: Mantle-derived oxide xenoliths from a hydrogen-rich environment. *Lithos* **2020**, *358–359*, 105404. [CrossRef]
12. Griffin, W.L.; Gain, S.E.M.; Adams, D.T.; Huang, J.-X.; Saunders, M.; Toledo, V.; Pearson, N.J.; O'Reilly, S.Y. First terrestrial occurrence of tistarite (Ti_2O_3): Ultra-low oxygen fugacity in the upper mantle beneath Mt Carmel, Israel. *Geology* **2016**, *44*, 815–818. [CrossRef]
13. Griffin, W.; Gain, S.; Huang, J.-X.; Belousova, E.; Toledo, V.; O'Reilly, S. Permian to quaternary magmatism beneath the Mt Carmel area, Israel: Zircons from volcanic rocks and associated alluvial deposits. *Lithos* **2018**, *314–315*, 307–322. [CrossRef]
14. Griffin, W.L.; Gain, S.E.M.; Bindi, L.; Toledo, V.; Cámara, F.; Saunders, M.; O'Reilly, S.Y. Carmeltazite, $ZrAl_2Ti_4O_{11}$, a new mineral trapped in corundum from volcanic rocks of Mt Carmel, northern Israel. *Minerals* **2018**, *8*, 601. [CrossRef]
15. Griffin, W.L.; Gain, S.E.M.; Saunders, M.; Bindi, L.; Alard, O.; Toledo, V.; O'Reilly, S.Y. Parageneses of TiB_2 in corundum xenoliths from Mt Carmel, Israel: Siderophile behaviour of Boron under reducing conditions. *Am. Mineral.* **2021**, *105*, 1609–1621. [CrossRef]
16. Griffin, W.L.; Gain, S.E.M.; Huang, J.-X.; Alard, O.; Toledo, V.; O'Reilly, S.Y. Immiscible metallic melts in the upper mantle beneath Mount Carmel, Israel: Silicides, phosphides and carbides. *Am. Mineral.* **2021**, in press.

17. Huang, J.-X.; Xiong, Q.; Gain, S.E.; Griffin, W.L.; Murphy, T.D.; Shiryaev, A.A.; Li, L.; Toledo, V.; Tomshin, M.D.; O'Reilly, S.Y. Immiscible metallic melts in the deep Earth: Clues from moissanite (SiC) in volcanic rocks. *Sci. Bull.* **2020**, *65*, 1479–1488. [CrossRef]
18. Griffin, W.L.; Gain, S.E.M.; Saunders, M.; Cámara, F.; Bindi, L.; Spartà, D.; Toledo, V.; O'Reilly, S.Y. Cr_2O_3 in Corundum: Ultra-high contents under reducing conditions. *Am. Mineral.* **2021**, in press.
19. Litasov, K.D.; Kagi, H.; Bekker, T.B. Enigmatic super-reduced phases in corundum from natural rocks: Possible contamination from artificial abrasive materials or metallurgical slags. *Lithos* **2019**, *340–341*, 181–190. [CrossRef]
20. Griffin, W.L.; Huang, J.; Thomassot, E.; Gain, S.E.M.; Toledo, V.; O'Reilly, S.Y. Super-reducing conditions in ancient and modern volcanic systems: Sources and behaviour of carbon-rich fluids in the lithospheric mantle. *Mineral. Petrol.* **2018**, *112* (Suppl. 1), 101–114. [CrossRef]
21. Oliveira, B.; Griffin, W.L.; Gain, S.E.M.; Saunders, M.; Shaw, J.; Toledo, V.; Afonso, J.C.; O'Reilly, S.Y. Ti^{3+} in corundum traces crystal growth in a highly reduced magma. *Sci. Rep.* **2021**, *11*, 2439. [CrossRef]
22. Bindi, L.; Cámara, F.; Griffin, W.L.; Huang, J.-X.; Gain, S.E.; Toledo, V.; O'Reilly, S.Y. Discovery of the first natural hydride. *Am. Mineral.* **2019**, *104*, 611–614. [CrossRef]
23. Bindi, L.; Cámara, F.; Gain, S.E.M.; Griffin, W.L.; Huang, J.-X.; Saunders, M.; Toledo, V. Kishonite, VH_2, and oreillyite, Cr_2N, two new minerals from the corundum xenocrysts of Mt Carmel, Northern Israel. *Minerals* **2020**, *10*, 1118. [CrossRef]
24. Roedder, E. Origin of fluid inclusions and changes that occur after trapping. In *Fluid Inclusions: Applications to Petrology*; Hollister, L.S., Crawford, M.L., Eds.; Mineralogical Association of Canada Short Courses: Calgary, AB, Canada, 1981; Volume 6, pp. 101–137.
25. Rees, K.; Lorusso, E.; Cosham, S.D.; Hyett, G.; Kulak, A.N. Combining single source chemical vapour deposition precursors to explore the phase space of titanium oxynitride thin films. *Dalton Trans.* **2018**, *47*, 10536–10543. [CrossRef]
26. Tkachuk, O.; Matychak, Y.; Pohrelyuk, I.; Fedirko, V. Diffusion of nitrogen and phase-structural transformations in titanium. *Metallofiz. Noveishie. Tekhnol.* **2016**, *36*, 1079–1089. [CrossRef]
27. Wreidt, H.A.; Murray, J.L. The N-Ti (Nitrogen-Titanium) system. *Bull. Alloy. Phase Diagr.* **1987**, *8*, 378–388. [CrossRef]
28. Khidirov, I. Revision of the Ti-N phase diagram as probed by neutron diffraction. *Russ. J. Inorg. Chem.* **2011**, *56*, 298–303. [CrossRef]
29. Roskosz, M.; Bouhifd, M.A.; Jephcoat, A.; Marty, B.; Mysen, B. Nitrogen solubility in molten metal and silicate at high pressure and temperature. *Geochim. Cosmochim. Acta* **2013**, *121*, 15–28. [CrossRef]
30. Mysen, B.O.; Yamashita, S.; Chertkova, N. Solubility and solution mechanisms of NOH volatiles in silicate melts at high pressure and temperature—Amine groups and hydrogen fugacity. *Am. Mineral.* **2008**, *93*, 1760–1770. [CrossRef]
31. Kadik, A.A.; Litvin, Y.A.; Koltashev, V.V.; Kryukova, E.B.; Plotnichenko, V.G.; Tsekhonya, T.I.; Kononkova, N.N. Solution behavior of reduced N–H–O volatiles in FeO–Na_2O–SiO_2–Al_2O_3 melt equilibrated with molten Fe alloy at high pressure and temperature. *Phys. Earth Planet. Inter.* **2013**, *214*, 14–24. [CrossRef]
32. Libourel, G.; Marty, B.; Humbert, F. Nitrogen solubility in basaltic melt. Part I. Effect of oxygen fugacity. *Geochim. Cosmochim. Acta* **2003**, *67*, 4123–4135. [CrossRef]
33. Speelmanns, I.M.; Schmidt, M.W.; Liebske, C. Nitrogen solubility in core materials. *Geophys. Res. Lett.* **2018**, *45*, 7434–7443. [CrossRef]
34. Liu, J.; Dorfman, S.; Lv, M.; Zhu, F.; Kono, Y. Loss of immiscible nitrogen from metallic melt explains Earth's missing nitrogen. *Geochem. Perspect. Lett.* **2019**, *11*, 18–22. [CrossRef]
35. Kadik, A.A.; Kurovskaya, N.A.; Ignat'Ev, Y.A.; Kononkova, N.N.; Koltashev, V.V.; Plotnichenko, V.G. Influence of oxygen fugacity on the solubility of nitrogen, carbon, and hydrogen in FeO-Na_2O-SiO_2-Al_2O_3 melts in equilibrium with metallic iron at 1.5 GPa and 1400 °C. *Geochem. Internat.* **2011**, *49*, 429–438. [CrossRef]
36. Martinez, I.; Javoy, M. The stability of nitrides in meteorites and in the Earth's mantle: A thermodynamic and experimental study. *Mineral. Mag.* **1998**, *62*, 955–956. [CrossRef]
37. Neumann, G.; Kieffer, R.; Ettmayer, P. Uber das System TiC-TiN-TiO. *Monatsh. Chem.* **1972**, *103*, 130–1137. [CrossRef]
38. Fukai, Y. *The Metal-Hydrogen System: Basic Bulk Properties*; Springer: Berlin/Heidelberg, Germany, 2006; Volume 21, p. 497.
39. Do, H.; Yen, T.-C.; Chang, L. Stability and etching of titanium oxynitride films in hydrogen microwave plasma. *J. Vac. Sci. Technol. A* **2013**, *31*, 041304. [CrossRef]